Electronic Supplementary Material (ESI) for Journal of Materials Chemistry C.
This journal is © The Royal Society of Chemistry 2019

SUPPORTING INFORMATION

Humidity driven molecular switch based on photoluminescent Dy^{III}Co^{III} single-molecule magnet

Szymon Chorazy,*[,a] Jakub J. Zakrzewski,[a] Mateusz Reczyński, [a] Koji Nakabayashi,[b]
Shin-ichi Ohkoshi,*[,b] and Barbara Sieklucka[a]

[a] Faculty of Chemistry, Jagiellonian University, Gronostajowa 2, 30-387 Kraków, Poland. [b] Department of Chemistry, School of Science, The University of Tokyo, 7-3-1 Hongo, Bunkyo-ku, Tokyo 113-0033, Japan.

*Corresponding authors: chorazy@chemia.uj.edu.pl; ohkoshi@chem.s.u-tokyo.ac.jp

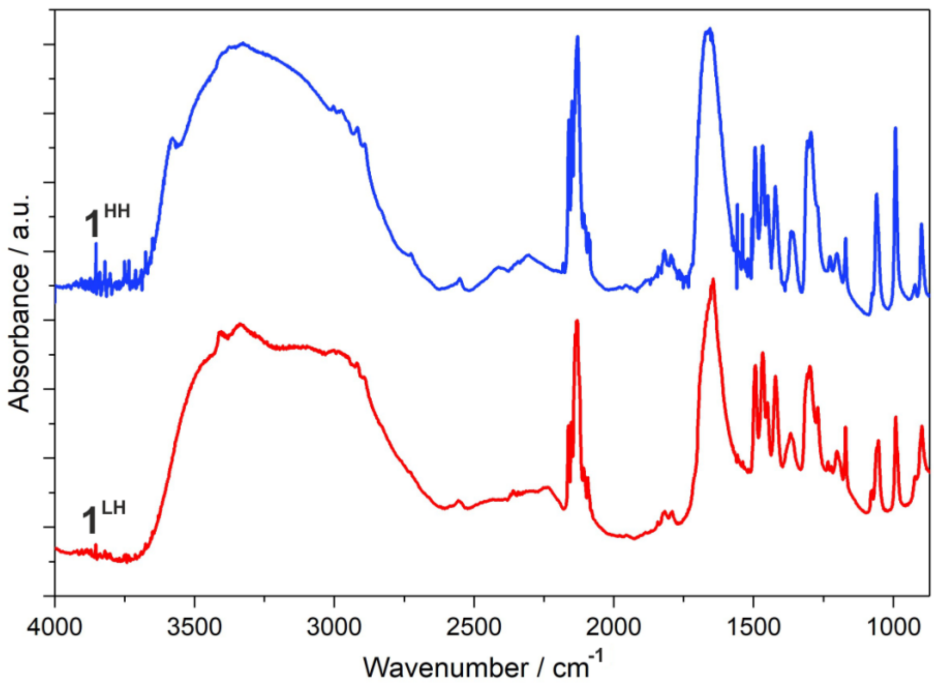

Figure S1. Infrared absorption spectra of the selected single crystals of **1**$^{\mathbf{HH}}$ and **1**$^{\mathbf{LH}}$.

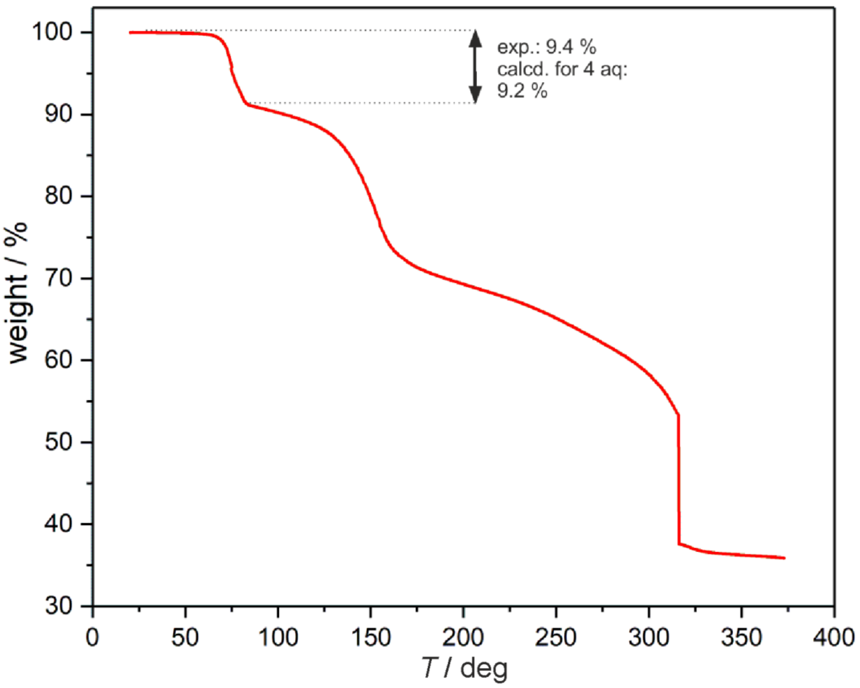

Figure S2. Thermogravimetric curve of **1**$^{\mathbf{LH}}$ collected in the temperature range of 20–375 °C. The steps related to the loss of water molecules were depicted. The experiments were conducted under an air atmosphere with the heating rate of 1 °C per minute.

Table S1. Crystal data and structure refinement for $\mathbf{1}^{\mathbf{HH}}$ and $\mathbf{1}^{\mathbf{LH}}$.

compound		$\mathbf{1}^{\mathbf{HH}}$	$\mathbf{1}^{\mathbf{LH}}$
method		single-crystal XRD	
formula		$Dy_1Co_1C_{22}H_{38}N_{10}O_9$	$Dy_1Co_1C_{22}H_{36}N_{10}O_8$
formula weight [g·mol^{-1}]		808.05	790.04
T [K]		200(2)	
λ [Å]		0.71075	
crystal system		triclinic	
space group		$P\bar{1}$	
unit cell	a [Å]	9.0161(5)	9.0316(8)
	b [Å]	12.1545(9)	12.0690(11)
	c [Å]	14.2631(8)	14.0244(11)
	α [deg]	90.320(6)	95.225(7)
	β [deg]	92.439(6)	90.460(6)
	γ [deg]	91.052(6)	90.216(6)
V [Å^3]		1561.33(17)	1522.3(2)
Z		2	2
calculated density [g·cm^{-3}]		1.719	1.724
absorption coefficient [cm^{-1}]		2.969	3.040
$F(000)$		810	790
crystal size [mm × mm × mm]		0.15 × 0.08 × 0.07	
crystal type		colourless plate	
θ range [deg]		3.096-25.028	3.101-25.023
limiting indices		$-10 < h < 10$ $-14 < k < 14$ $-16 < l < 16$	
collected reflections		11969	11466
unique reflections		5431	5308
R_{int}		0.0671	0.0853
completeness [%]		98.4	98.8
max. and min. transmission		1.000 and 0.485	1.000 and 0.4605
data/restraints/parameters		5431/21/430	5308/13/415
GOF on F^2		1.143	1.171
final R indices		$R_1 = 0.0627$ [$I > 2\sigma(I)$] $wR_2 = 0.1029$ (all)	$R_1 = 0.0948$ [$I > 2\sigma(I)$] $wR_2 = 0.1547$ (all)
largest diff peak/hole [e·Å^{-3}]		1.761/-1.647	2.404/-2.858

Table S2. Detailed structure parameters of hexacyanidocobaltate(III) complexes in $\mathbf{1}^{\mathbf{HH}}$ and $\mathbf{1}^{\mathbf{LH}}$.

parameter	$\mathbf{1}^{\mathbf{HH}}$	$\mathbf{1}^{\mathbf{LH}}$
Co1-C1	1.905(10) Å	1.914(13) Å
Co1-C2	1.926(10) Å	1.902(16) Å
Co1-C3	1.896(9) Å	1.904(13) Å
Co1-C4	1.900(10) Å	1.913(16) Å
Co1-C5	1.883(8) Å	1.901(13) Å
Co1-C6	1.893(9) Å	1.886(13) Å
C1-N1	1.140(11) Å	1.142(15) Å
C2-N2	1.132(11) Å	1.153(17) Å
C3-N3	1.145(10) Å	1.142(15) Å
C4-N4	1.140(11) Å	1.166(17) Å
C5-N5	1.152(10) Å	1.136(14) Å
C6-N6	1.153(11) Å	1.161(16) Å
Co1-C1-N1	177.5(8) °	175.7(12) °
Co1-C2-N2	175.5(8) °	178.2(12) °
Co1-C3-N3	174.9(8) °	177.4(13) °
Co1-C4-N4	178.2(8) °	174.8(12) °
Co1-C5-C5	177.2(8) °	178.1(11) °
Co1-C6-N6	178.7(8) °	177.8(13) °
C1-Co1-C2	87.9(4) °	87.0(6) °
C1-Co1-C3	91.2(4) °	93.0(5) °
C1-Co1-C4	90.5(4) °	89.9(6) °
C1-Co1-C5	89.9(3) °	89.6(5) °
C1-Co1-C6	177.9(4) °	178.3(6) °
C2-Co1-C3	93.3(4) °	92.0(5) °
C2-Co1-C4	178.4(4) °	176.9(6) °
C2-Co1-C5	91.1(3) °	89.7(5) °
C2-Co1-C6	89.9(4) °	92.0(6) °
C3-Co1-C4	87.1(4) °	88.3(5) °
C3-Co1-C5	175.5(4) °	177.0(6) °
C3-Co1-C6	88.7(4) °	88.3(5) °
C4-Co1-C5	88.5(3) °	90.1(5) °
C4-Co1-C6	91.6(4) °	91.2(6) °
C5-Co1-C6	90.4(4) °	89.1(5) °
Co1-Dy1 distance	5.40(2) Å	5.41(3) Å

Table S3. Detailed structure parameters of dysprosium(III) complexes in $\mathbf{1}^{\mathbf{HH}}$ and $\mathbf{1}^{\mathbf{LH}}$.

parameter	$\mathbf{1}^{\mathbf{HH}}$	$\mathbf{1}^{\mathbf{LH}}$
Dy1-N1	2.447(7) Å	2.423(11) Å
Dy1-O1	2.404(6) Å	2.461(10) Å
Dy1-O2	2.391(6) Å	2.348(10) Å
Dy1-O3	2.383(7) Å	2.362(9) Å
Dy1-O4	2.325(7) Å	2.366(10) Å
Dy1-O5	2.322(6) Å	2.329(9) Å
Dy1-O6	2.375(6) Å	2.359(8) Å
Dy1-O7	2.312(6) Å	2.296(9) Å
N1-Dy1-O1	141.5(2) °	141.8(3) °
N1-Dy1-O2	95.3(2) °	92.8(4) °
N1-Dy1-O3	84.5(3) °	86.7(4) °
N1-Dy1-O4	88.9(3) °	89.6(4) °
N1-Dy1-O5	72.2(2) °	74.7(3) °
N1-Dy1-O6	73.6(2) °	73.6(3) °
N1-Dy1-O7	149.0(2) °	148.7(3) °
O1-Dy1-O2	76.4(2) °	72.1(4) °
O1-Dy1-O3	124.2(2) °	117.5(4) °
O1-Dy1-O4	81.1(2) °	85.3(3) °
O1-Dy1-O5	69.5(2) °	67.3(3) °
O1-Dy1-O6	136.5(2) °	140.6(3) °
O1-Dy1-O7	68.1(2) °	68.4(3) °
O2-Dy1-O3	68.1(2) °	68.5(3) °
O2-Dy1-O4	148.7(2) °	146.1(3) °
O2-Dy1-O5	72.8(2) °	71.3(3) °
O2-Dy1-O6	137.0(2) °	136.2(3) °
O2-Dy1-O7	103.4(2) °	109.3(4) °
O3-Dy1-O4	143.2(2) °	145.4(3) °
O3-Dy1-O5	131.8(2) °	134.4(4) °
O3-Dy1-O6	69.58(19) °	69.4(3) °
O3-Dy1-O7	79.9(2) °	81.4(4) °
O4-Dy1-O5	79.1(2) °	76.8(3) °
O4-Dy1-O6	73.9(2) °	76.6(3) °
O4-Dy1-O7	87.8(3) °	84.2(4) °
O5-Dy1-O6	136.3(2) °	138.3(3) °
O5-Dy1-O7	137.0(2) °	132.7(3) °
O6-Dy1-O7	75.9(2) °	75.1(3) °

Table S4. Donor-acceptor distances in the hydrogen bonding network of $\mathbf{1^{HH}}$ and $\mathbf{1^{LH}}$.

donor-H···acceptor	$\mathbf{1^{HH}}$	$\mathbf{1^{LH}}$
O2-H2B···N2	2.87(1) Å	2.82(2) Å
O3-H3A···N2	2.88(1) Å	2.88(2) Å
O2-H2A··· N3	2.817(9) Å	2.80(2) Å
O1S-H1B···N4	2.79(1) Å	2.78(2) Å
N11-H11···N5	3.14(1) Å	3.13(2) Å
O3-H3B··· N5	2.779(9) Å	2.73(1) Å
O1S-H1A···N6	2.87(1) Å	2.85(1) Å
N8-H8···O1	3.01(1) Å	2.97(2) Å
N11-H11···O6	3.03(1) Å	3.00(2) Å
O1-H1D···O1S	2.733(9) Å	2.64(1) Å
N10-H10···O4	2.88(1) Å	3.02(2) Å
N9-H9···N3 → N9-H9···N4*	3.20(1) Å	3.49(2) Å
O1-H1C···O2S → O1-H1C···N3*	2.715(9) Å	3.03(2) Å
O2S-H2C···N3*	3.25(1) Å	–
N8-H8···O2S*	3.08(1) Å	–
O2S-H2D···O1S*	2.92(1) Å	–

* The hydrogen bonds involving O2S disappear in $\mathbf{1^{LH}}$ as the related water molecule is removed from the crystal structure. In addition, the N9-H9···N3 bond is replaced by the N9-H9···N4 contact, while the O1-H1C···N3 hydrogen bond replaces the O1-H1C···O2S contact, both due to the dehydration-induced reorientation the 2-pyrrolidone ligands and slight movement of the cyanide ligands.

Table S5. Results of Continuous Shape Measure Analysis for $[Dy(2\text{-pyrrolidone})_4(H_2O)_3(NC)]^{2+}$ complexes in the crystal structures of $\mathbf{1^{HH}}$ and $\mathbf{1^{LH}}$.

compound	CSM parameters*			geometry
	SAPR-8	DD-8	BTP-8	
$\mathbf{1^{HH}}$	3.038	1.063	1.689	DD-8
$\mathbf{1^{LH}}$	2.735	1.798	1.381	BTP-8

* CSM parameters:
CSM BTP-8 = the parameter related to the bicapped trigonal prism geometry (C_{2v} symmetry)
CSM SAPR-8 = the parameter related to the square antiprism (D_{4d} symmetry)
CSM DD-8 = the parameter related to the dodecahedron (D_{2d} symmetry)
CSM = 0 for the ideal geometry and the increase of CSM parameter corresponds to the increasing distortion from the ideal polyhedron.

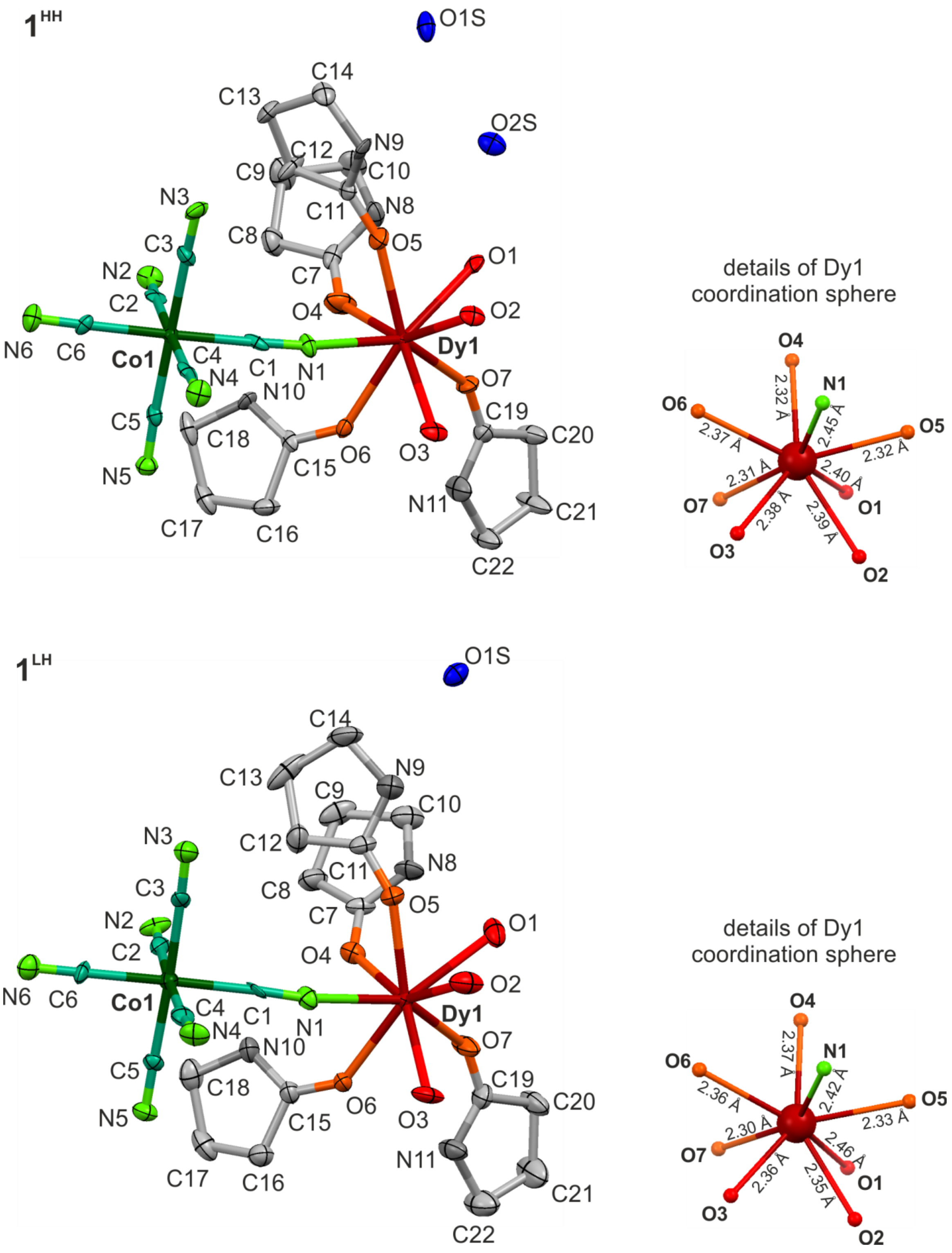

Figure S3. Comparison of the asymmetric units of $\mathbf{1}^{\mathbf{HH}}$ and $\mathbf{1}^{\mathbf{LH}}$ with the atoms labelling schemes, and the detailed insight into the coordination spheres of Dy1 complexes. Thermal ellipsoids are presented at the 50% probability level. The related bond lengths and angles are collected in Tables S2–S3. Hydrogen atoms were omitted for clarity.

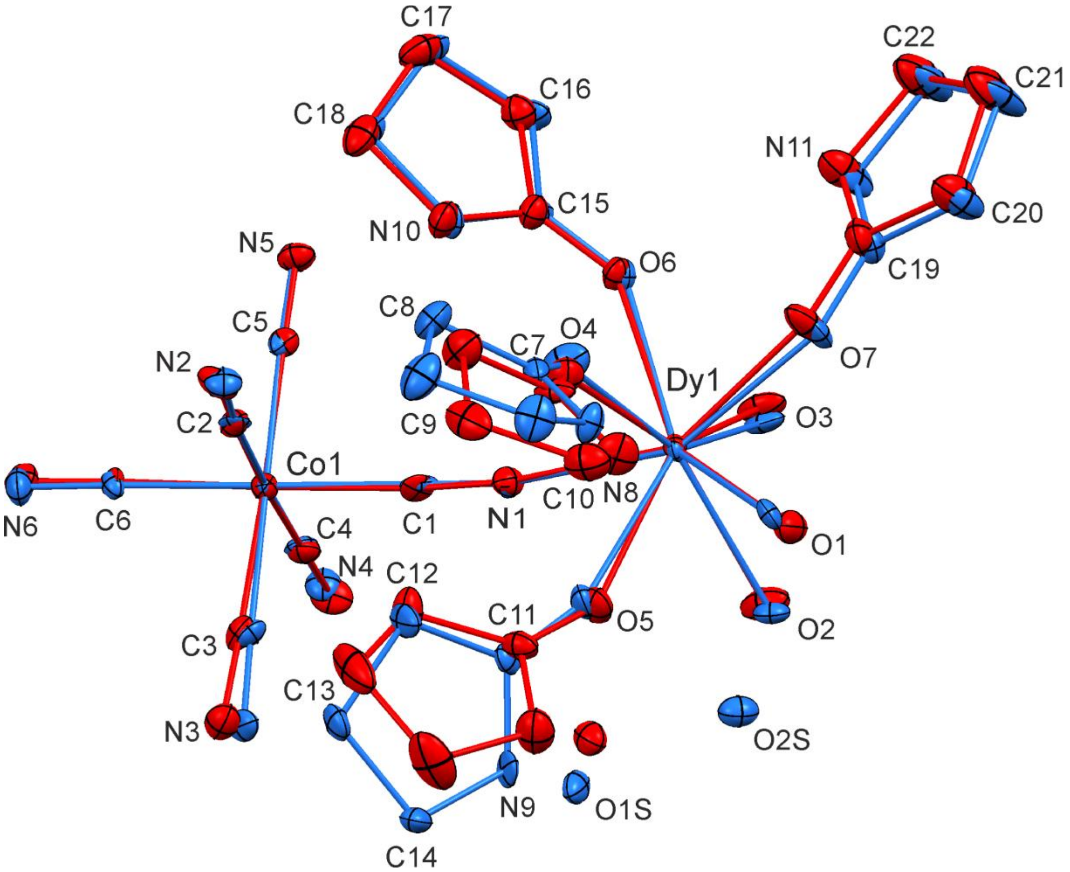

Figure S4. View of the overlapping asymmetric units of **1**$^{\mathbf{HH}}$ (blue) and **1**$^{\mathbf{LH}}$ (red) showing the changes of the crystal structure upon the humidity driven phase transformation. Thermal ellipsoids are presented at the 25% probability level. The atoms labelling scheme was shown to compare the related bond lengths and angles which are collected in Tables S2–S3. Hydrogen atoms were omitted for clarity.

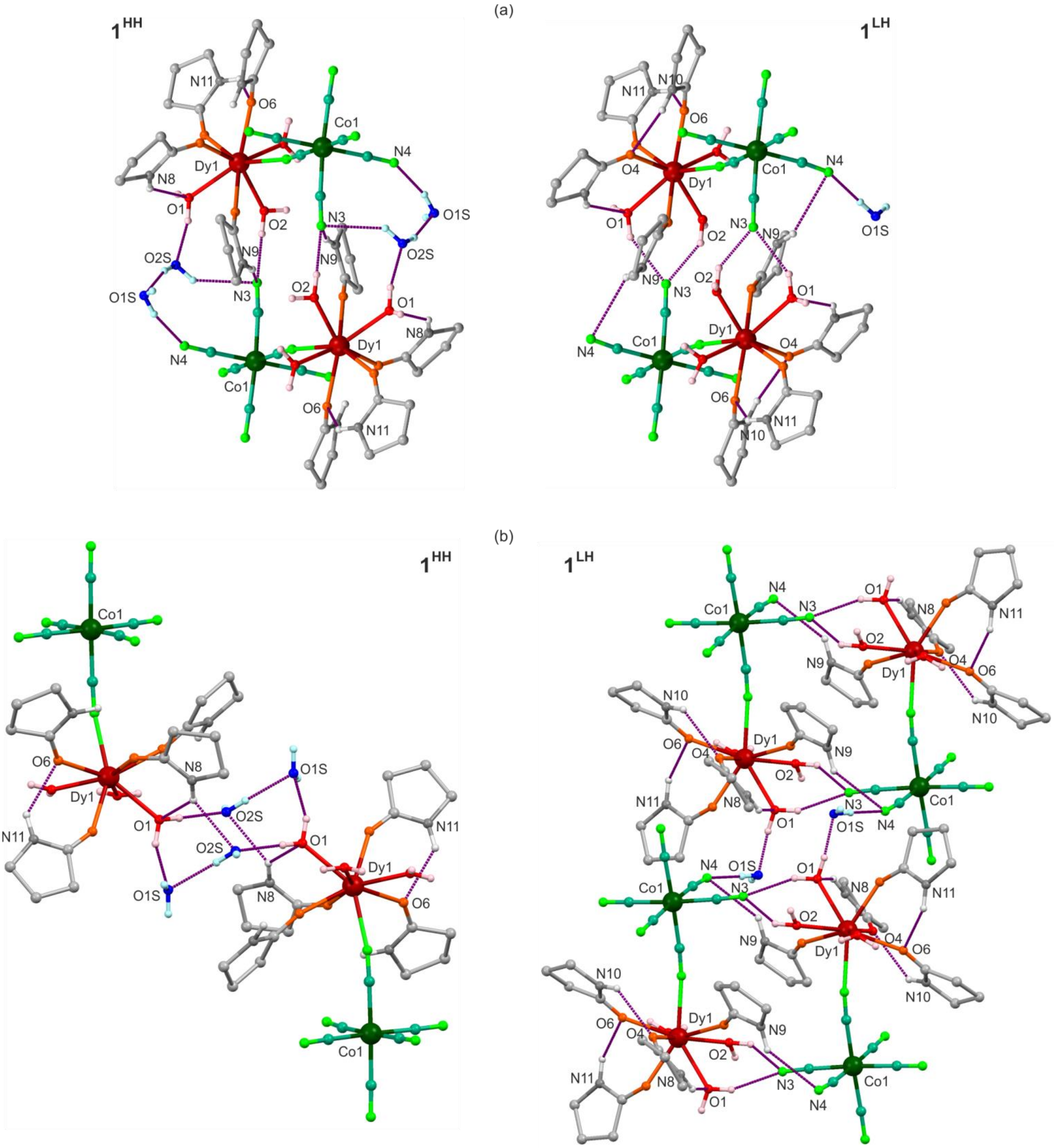

Figure S5. Detailed views of the hydrogen bonds within the supramolecular networks of $\mathbf{1}^{\mathbf{HH}}$ (left panel) and $\mathbf{1}^{\mathbf{LH}}$ (right panel) with the insight into the non-covalent interactions between pairs of neighbouring {DyCo} molecules (*a*), and the insight into the Dy–Dy supramolecular interactions through crystallization water molecules (*b*). The hydrogen bonds were presented as violet lines.

Comment to Figures 1 and S3–S5.

Structural changes related to the dehydration-induced $\mathbf{1^{HH}}$ to $\mathbf{1^{LH}}$ transformation

The removal of the O2S water molecule results in slight relative shift of the {DyCo} units (ca. 0.64 Å along the direction of CN-bridges), which originates form the fitting of the molecules to the space left by the water molecule. This slight shift is accompanied by a significant rearrangement of the H-bond network. The H-bond interaction between the {DyCo} unit and the O2S water molecule (O1-H1C···O2S) in $\mathbf{1^{HH}}$ is replaced by an additional interaction with a neighbouring {DyCo} unit via a CN- ligand (O1-H1C···N3) in $\mathbf{1^{LH}}$. As a result, the C3-N3 cyanide ligand interacts with two aqua ligands (O1, O2) in the coordination sphere of the Dy ion in the next {DyCo} molecule, which is one of the factors that induce change in the coordination sphere. The pyron ligands are affected in a similar way. The most significant change in the Dy-O5 bond length after dehydration is observed for the ligand which donated the H-bond to the removed water molecule (N8-H8···O2S). Moreover, the removal of the O2S water and the related shifting of the {DyCo} molecules cuts off the H-bond path connecting two neighbouring Dy ions.

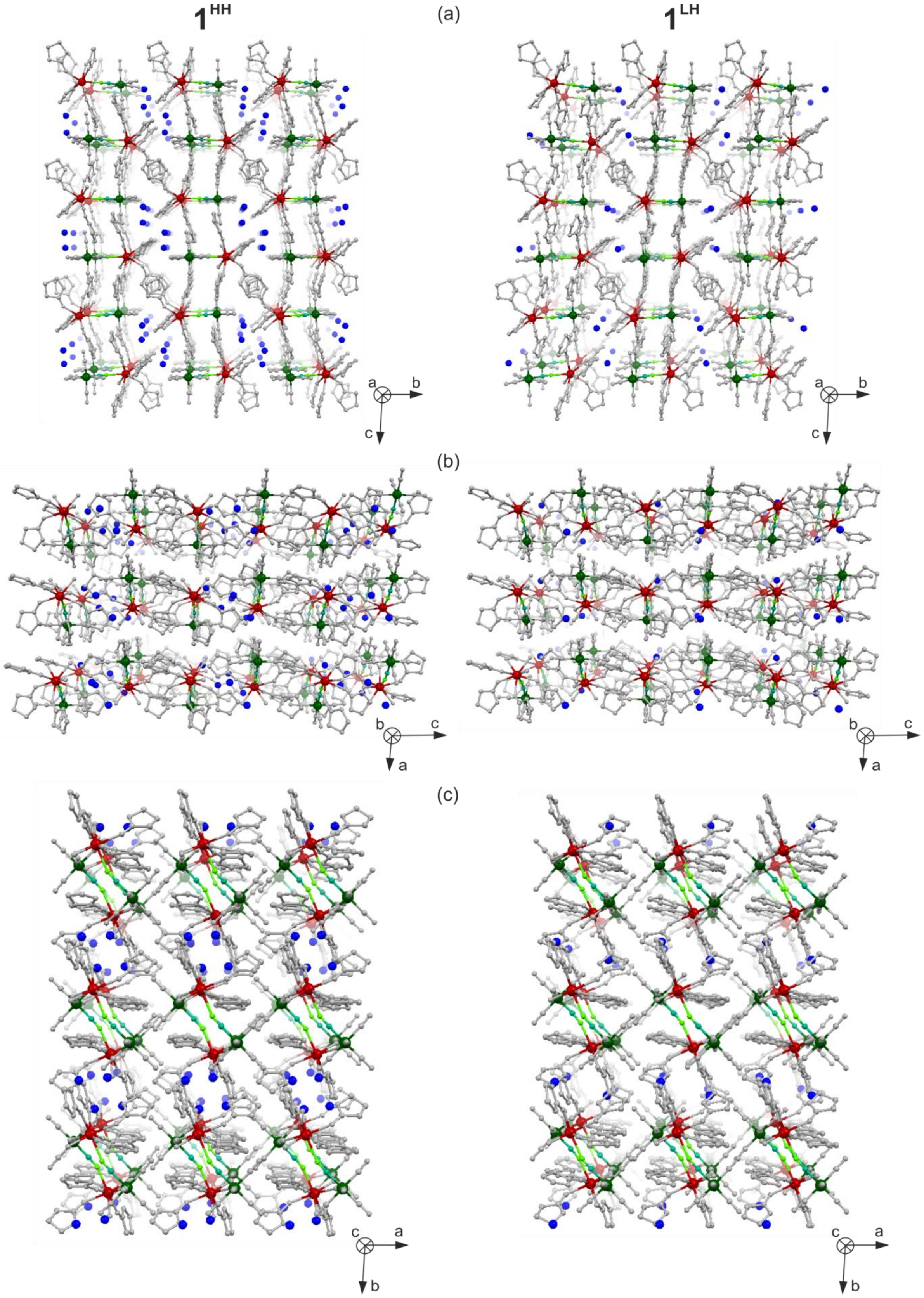

Figure S6. The views of the supramolecular arrangement of dinuclear molecules in $\mathbf{1}^{\mathbf{HH}}$ (left panel) and $\mathbf{1}^{\mathbf{LH}}$ (right panel) shown along the crystallographic ***a*** axis (*a*), ***b*** axis (*b*) and ***c*** axis (*c*).

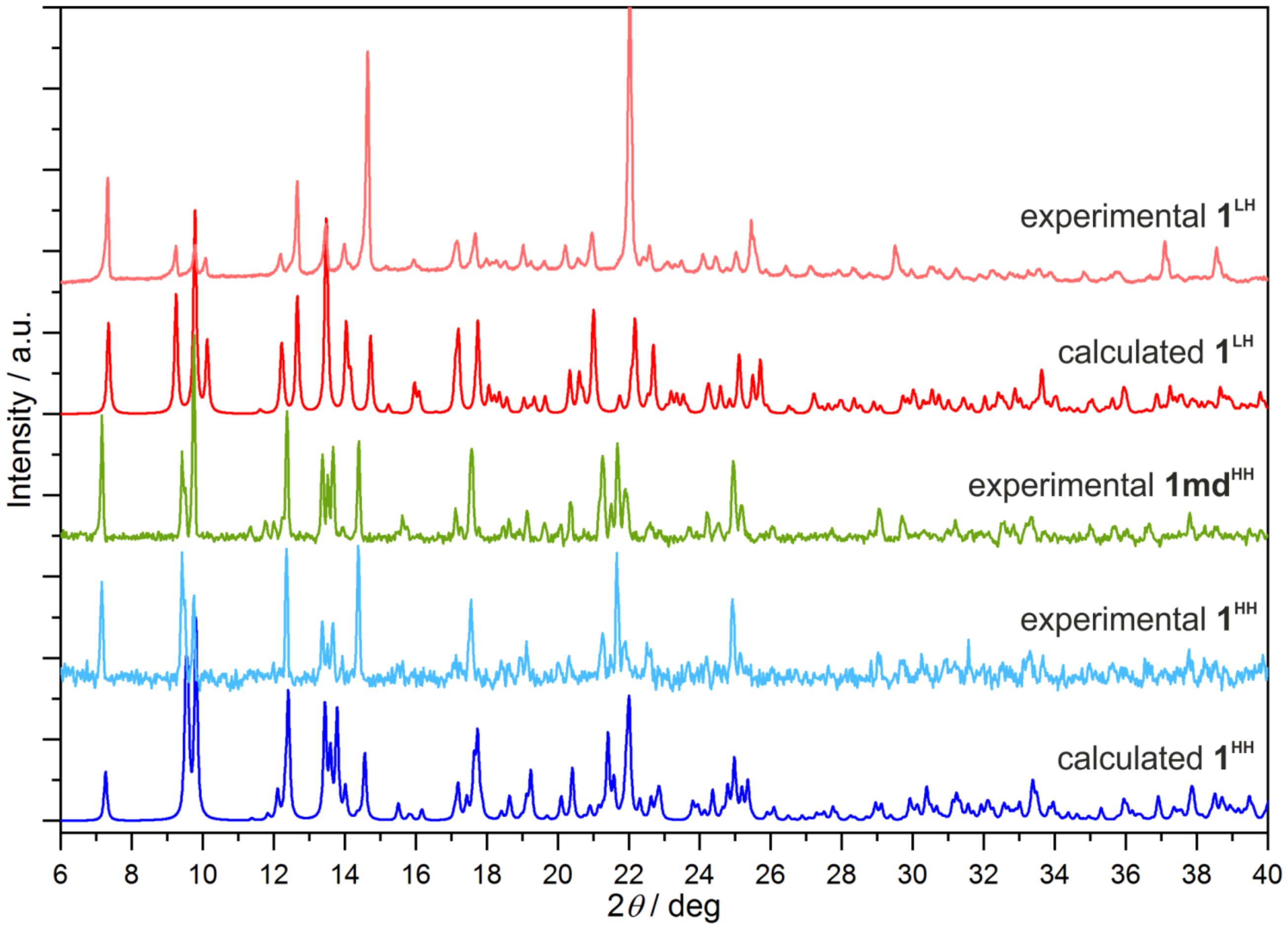

Figure S7. Experimental powder X-ray diffraction (PXRD) patterns of various crystalline phases of **1**: high humidity phase, $\mathbf{1}^{\mathbf{HH}}$, low humidity phase, $\mathbf{1}^{\mathbf{LH}}$, and magnetically diluted high humidity phase, $\mathbf{1md}^{\mathbf{HH}}$. For comparison, the PXRD pattern calculated from the structural models of $\mathbf{1}^{\mathbf{LH}}$ and $\mathbf{1}^{\mathbf{HH}}$ obtained within the single crystal X-ray diffraction structural analyses were also presented. Note that the experimental patterns of $\mathbf{1}^{\mathbf{HH}}$ and $\mathbf{1md}^{\mathbf{HH}}$ were gathered using a rotating capillary system, while the experimental pattern of $\mathbf{1}^{\mathbf{LH}}$ was collected on grinded sample using the standard horizontal holder, thus, this pattern contains the reflections intensities slightly disturbed by the effect of crystals' preferred orientation.

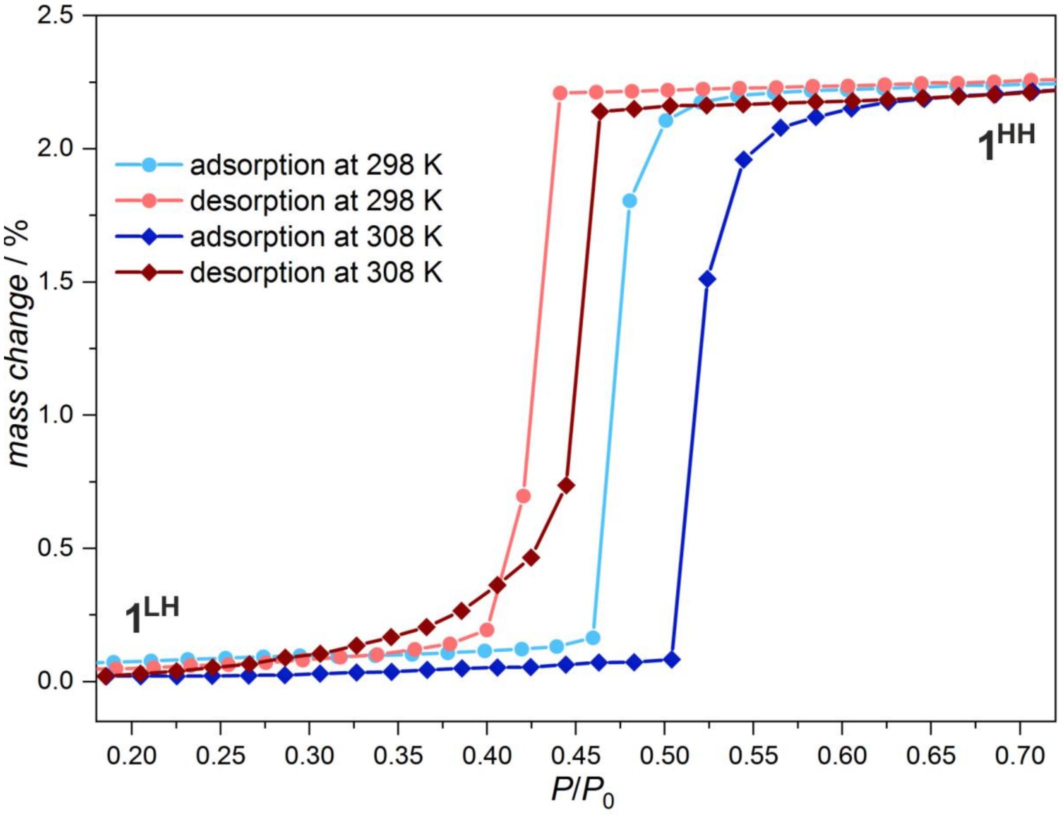

Figure S8. Water adsorption isotherms measured at room temperature (298 K) and the increased temperature of 308 K, showing the humidity driven switching between $\mathbf{1}^{\mathbf{HH}}$ and $\mathbf{1}^{\mathbf{LH}}$ phases under variable thermal conditions. The values of P/P_0 represent the relative humidity used for the stabilization of the sample mass at each point.

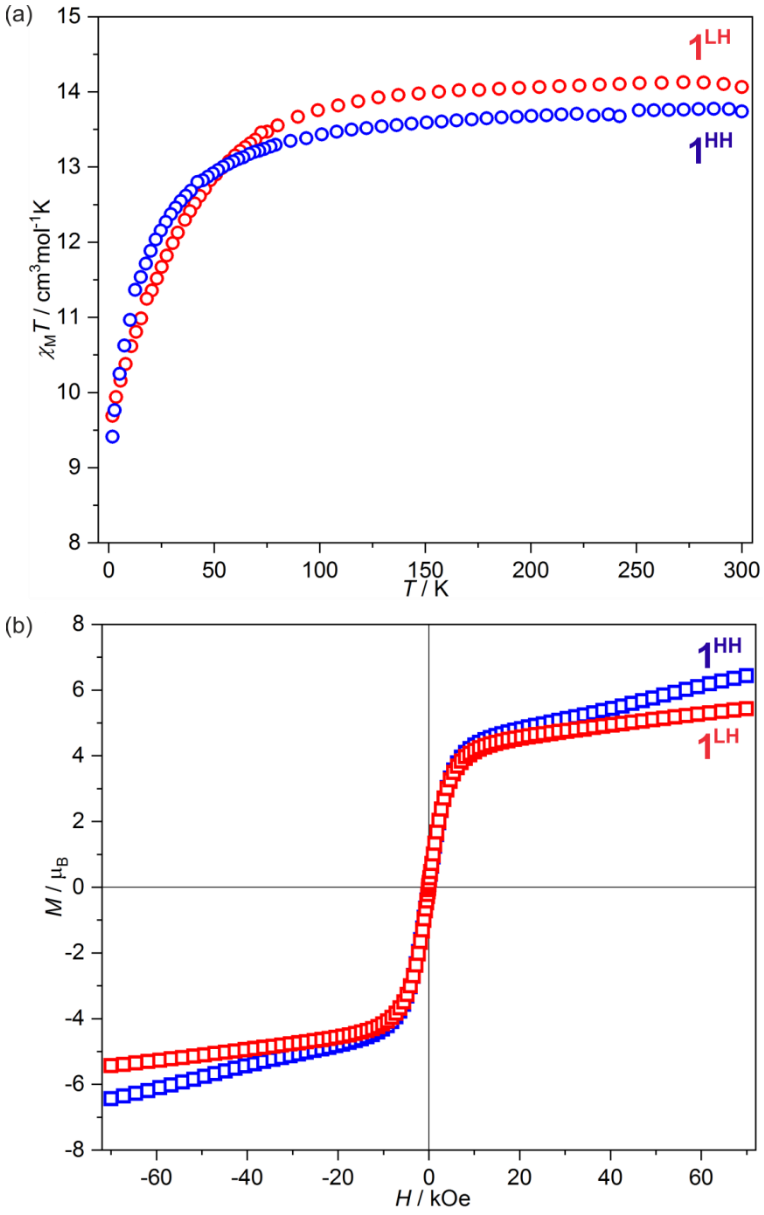

Figure S9. Direct-current (*dc*) magnetic properties of $\mathbf{1}^{\mathbf{HH}}$ (blue) and $\mathbf{1}^{\mathbf{LH}}$ (red): temperature dependences of the $\chi_M T$ product at H_{dc} = 1000 Oe (*a*), and the field dependences of molar magnetization, M at T = 1.8 K (*b*).

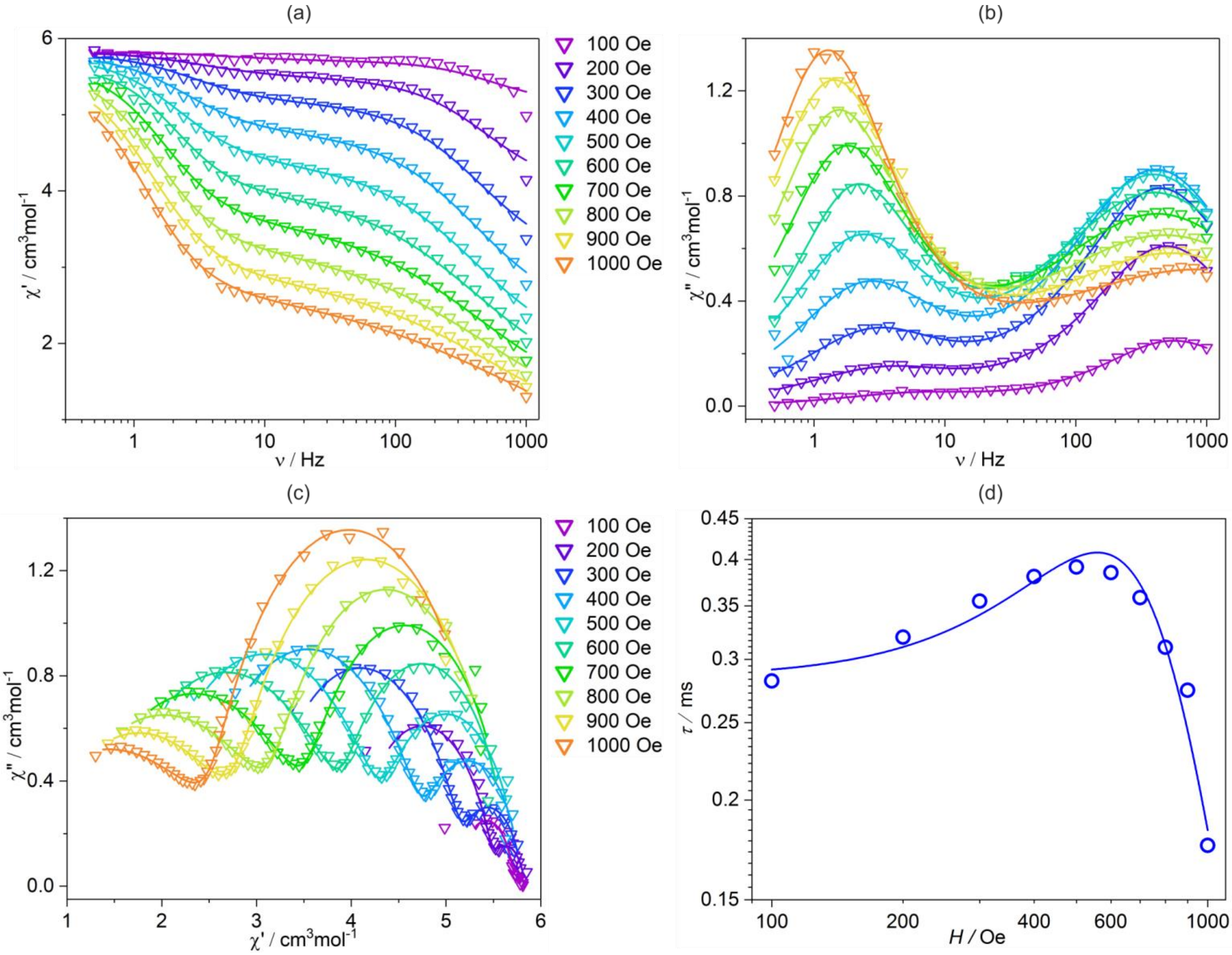

Figure S10. Complete magnetic-field-variable alternate-current (*ac*) magnetic susceptibility characteristics of **1**$^{\mathbf{HH}}$ at $T = 1.8$ K under $H_{\mathrm{ac}} = 1$ Oe, and their analysis: frequency dependences of the in-phase susceptibility, χ' (*a*), and the out-of-phase susceptibility, χ'' (*b*) at various indicated *dc* external magnetic fields, together with the related Argand plots (*c*), and the resulting field dependence of the relaxation time, τ (*d*). Both field and relaxation time were presented in (*d*) in the logarithmic scale. The relaxation times in (*d*) were shown for the faster relaxation process. Coloured solid curves in (*a*), (*b*), and (*c*) represent the best fits using the generalized Debye model for two relaxation processes. The solid line in (*d*) shows the best fit taking into account two contributions: quantum tunnelling of magnetization and a direct process, in the range of 100–1000 Oe (see comment on Page S17).

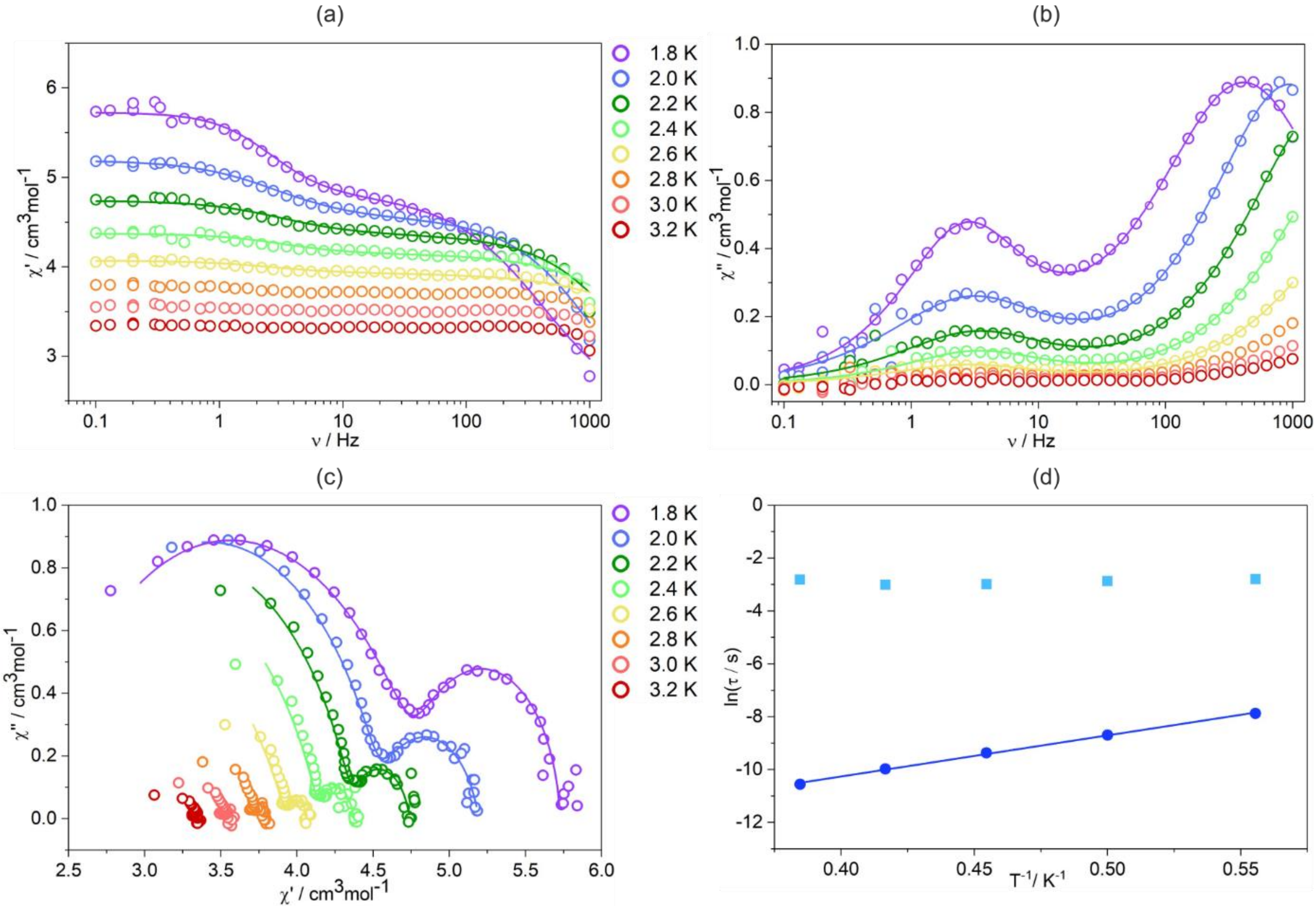

Figure S11. Complete temperature-variable alternate-current (*ac*) magnetic susceptibility characteristics of $\mathbf{1}^{\mathbf{HH}}$ under H_{ac} = 1 Oe, H_{dc} = 400 Oe, and their analysis: frequency dependences of the in-phase susceptibility, χ' (*a*), and the out-of-phase susceptibility, χ'' (*b*) at various indicated temperatures, together with the related Argand plots (*c*), and the temperature dependence of the relaxation time, τ (*d*). The relaxation times in (*d*) were shown for both the faster temperature-dependent relaxation (dark blue points), and the slower temperature-independent relaxation process (light blue points). Coloured solid curves in (*a*), (*b*), and (*c*) represent the best fits using the generalized Debye model for two relaxation processes. The solid line in (*d*) shows the best fit to the Arrhenius law ($\ln\tau = \ln\tau_0 - (U_{eff}/k_B)\cdot T^{-1}$) in the range of 1.8–2.6 K. The best-fit parameters are U_{eff}/k_B = 15.6(4) K with $\tau_0 = 6.9(8)\cdot 10^{-8}$ s.

Comment to Figures S10 and S11

For the fitting of the frequency dependences of χ’ and χ” contributions to the *ac* magnetic susceptibility, and the related Argand χ”(χ’) plots (Figures S10 and S11), the following equations (e1 and e2) of the generalized Debye model for two relaxation processes were used:

$$\chi'(\omega) = \chi_{S,total} + \Delta\chi_1 \frac{1+(\omega\tau_1)^{1-\alpha_1}\sin(\pi\alpha_1/2)}{1+2(\omega\tau_1)^{1-\alpha_1}\sin(\pi\alpha_1/2)+(\omega\tau_1)^{2(1-\alpha_1)}} + \Delta\chi_2 \frac{1+(\omega\tau_2)^{1-\alpha_2}\sin(\pi\alpha_2/2)}{1+2(\omega\tau_2)^{1-\alpha_2}\sin(\pi\alpha_2/2)+(\omega\tau_2)^{2(1-\alpha_2)}} \qquad \text{(e1)}$$

$$\chi''(\omega) = \Delta\chi_1 \frac{(\omega\tau_1)^{1-\alpha_1}\cos(\pi\alpha_1/2)}{1+2(\omega\tau_1)^{1-\alpha_1}\sin(\pi\alpha_1/2)+(\omega\tau_1)^{2(1-\alpha_1)}} + \Delta\chi_2 \frac{(\omega\tau_2)^{1-\alpha_2}\cos(\pi\alpha_2/2)}{1+2(\omega\tau_2)^{1-\alpha_2}\sin(\pi\alpha_2/2)+(\omega\tau_2)^{2(1-\alpha_2)}} \qquad \text{(e2)}$$

where

$\chi_{S,total}$ = the sum of the adiabatic susceptibilities of two separate relaxation processes ($\chi_{S,1} + \chi_{S,2}$),

$\Delta\chi_1$ = the difference between the adiabatic susceptibility ($\chi_{S,1}$) and the isothermal susceptibility ($\chi_{T,1}$) of the first relaxation process,

$\Delta\chi_2$ = the difference between the adiabatic susceptibility ($\chi_{S,2}$) and the isothermal susceptibility ($\chi_{T,2}$) of the second relaxation process,

τ_1 and τ_2 = the relaxation times of the first and the second relaxation processes, respectively,

α_1 and α_2 = the distribution (Cole-Cole) parameters of the first and the second relaxation processes, respectively, and ω is an angular frequency, that is $\omega = 2\pi v$, with v stands for the linear frequency in [Hz] units.[S1]

Results of the fittings according to the Debye model for two relaxation processes for **1$^{\mathbf{HH}}$** are shown in Figures S10(*a–c*) and S11(*a–c*). The resulting relaxation times (τ) were plotted against *dc* magnetic field (Figure S10d) under constant temperature of 1.8 K, and against temperature (Figure S11d) under constant *dc* field of 400 Oe.

[S1] (a) Y.-N. Guo, G.-F. Xu, Y. Guo and J. Tang, *Dalton Trans.*, 2011, **40**, 9956; (b) M. Ramos Silva, P. Martin-Ramos, J. T. Coutinho, L. C. J. Pereira and J. Martin-Gil, *Dalton Trans.*, 2014, **43**, 6752.

The τ versus H_{dc} dependence was fitted using the equation (e3):

$$\tau^{-1} = ATH^4 + a\left[\frac{(1+b^2H^2)}{(1+c^2H^2)}\right] \qquad \text{(e3)}$$

where the first term represented by the *A* parameter is related to the field-induced direct process, while the second term represented by the set of three parameters (*a*, *b*, *c*) is showing the contribution from quantum tunnelling of magnetization.[S2]

The result of the fitting for the τ versus H_{dc} dependence in **1$^{\mathbf{HH}}$** (Figure S10d) at T = 1.8 K: $A = 4.4(3)\cdot10^{-9}$ K^{-1} s^{-1} Oe^{-4}, a = 3513(177) s^{-1}, $b = 4.6(9)\cdot10^{-8}$ Oe^{-2}, and c = 0.0015(2) Oe^{-2}.

[S2] A. Amjad, A. Figuerola and L. Sorace, *Dalton Trans.*, 2017, **46**, 3848.

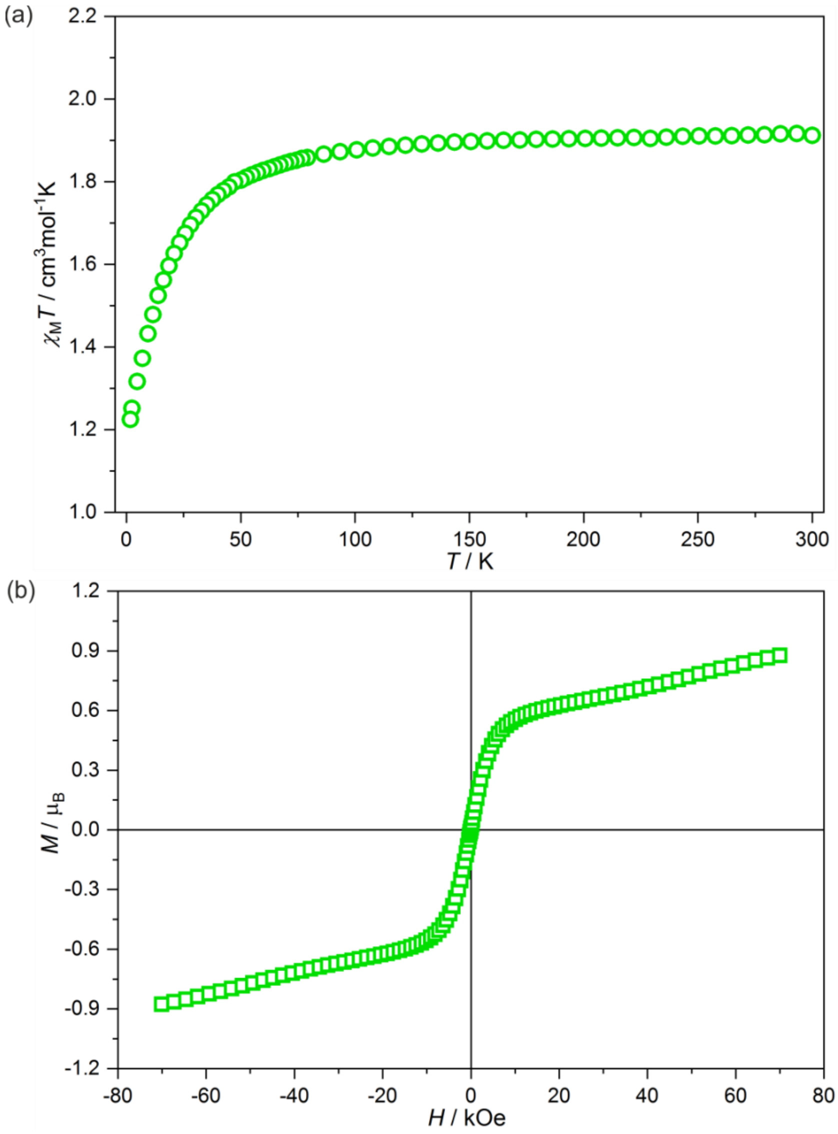

Figure S12. Direct-current (*dc*) magnetic properties of magnetically diluted high humidity phase, $\mathbf{1md^{HH}}$: the temperature dependence of $\chi_M T$ at H_{dc} = 1000 Oe (*a*), and the field dependence of molar magnetization, M measured at T = 1.8 K (*b*).

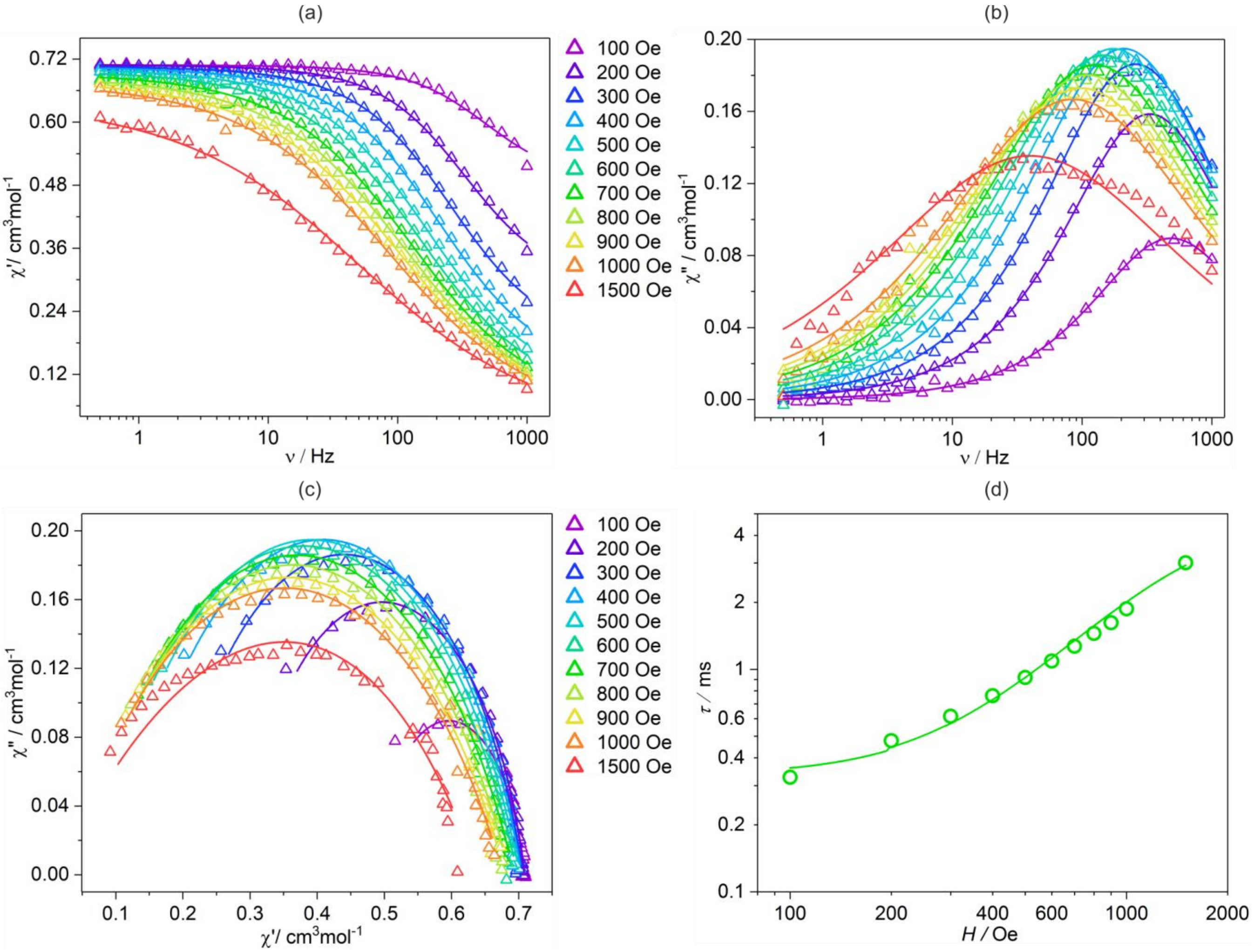

Figure S13. Complete magnetic-field-variable alternate-current (*ac*) magnetic susceptibility characteristics of **1md$^{\mathbf{HH}}$** at T = 1.8 K, under H_{ac} = 1 Oe, and their analysis: frequency dependences of the in-phase susceptibility, χ' (*a*), and the out-of-phase susceptibility, χ'' (*b*) at various indicated *dc* external magnetic fields, together with the related Argand plots (*c*), and the field dependence of the relaxation time, τ (*d*). Both field and relaxation time were presented in (*d*) in the logarithmic scale. Coloured solid curves in (*a*), (*b*), and (*c*) represent the best fits following the generalized Debye model for a single relaxation process. The solid line in (*d*) shows the best fit taking into account quantum tunnelling of magnetization, and a direct process, in the range of 100–1500 Oe (see comment on Page S21).

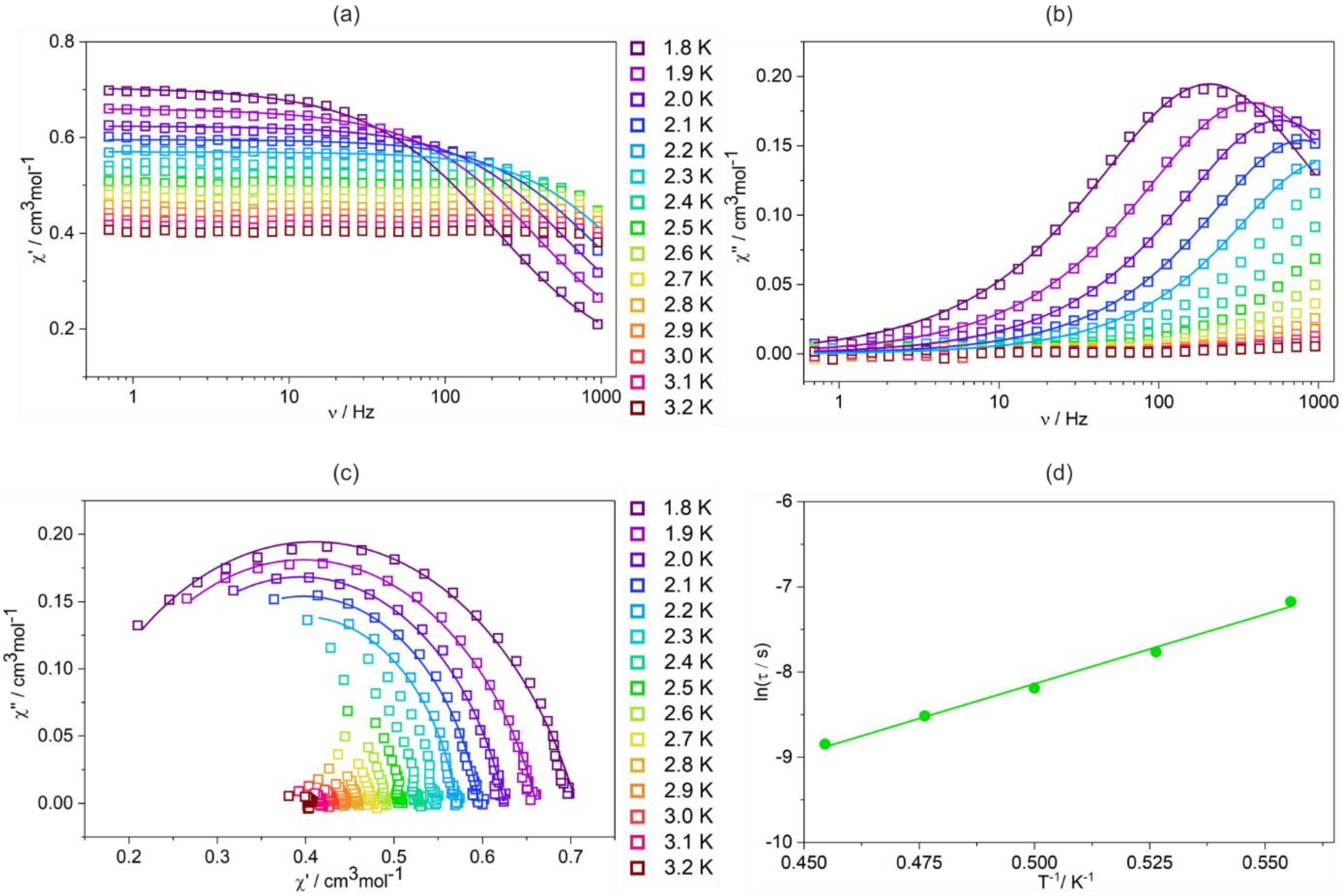

Figure S14. Complete temperature-variable alternate-current (*ac*) magnetic susceptibility characteristics of **1md$^{\mathbf{HH}}$** under H_{ac} = 1 Oe, H_{dc} = 400 Oe, and their analysis: frequency dependences of the in-phase susceptibility, χ' (*a*), and the out-of-phase susceptibility, χ'' (*b*) at various indicated temperatures, together with the related Argand plots (*c*), and the temperature dependence of the relaxation time, τ (*d*). Colored solid curves in (*a*), (*b*), and (*c*) represent the best fits using the generalized Debye model for a single relaxation process. The solid line in (*d*) shows the best fit to the Arrhenius law ($\ln\tau = \ln\tau_0 - (U_{\mathrm{eff}}/k_{\mathrm{B}})\cdot T^{-1}$) in the range of 1.8–2.2 K. The best-fit parameters are $U_{\mathrm{eff}}/k_{\mathrm{B}}$ = 16.3(7) K with $\tau_0 = 8.4(9)\cdot 10^{-8}$ s.

Comment to Figures S13 and S14

For the fitting of the frequency dependences of χ' and χ" contributions to the *ac* magnetic susceptibility, and the related Argand χ"(χ') plots (Figures S13 and S14), the following equations (e4 and e5) of the generalized Debye model for a single relaxation process were used:

$$\chi'(\omega) = \chi_S + (\chi_T - \chi_S)\frac{1+(\omega\tau)^{1-\alpha}\sin(\pi\alpha/2)}{1+2(\omega\tau)^{1-\alpha}\sin(\pi\alpha/2)+(\omega\tau)^{2(1-\alpha)}} \qquad \text{(e4)}$$

$$\chi''(\omega) = (\chi_T - \chi_S)\frac{(\omega\tau)^{1-\alpha}\cos(\pi\alpha/2)}{1+2(\omega\tau)^{1-\alpha}\sin(\pi\alpha/2)+(\omega\tau)^{2(1-\alpha)}} \qquad \text{(e5)}$$

where

χ_S = the adiabatic susceptibility (at infinitely high frequency of *ac* field),

χ_T = the isothermal susceptibility (at infinitely low frequency of *ac* field),

τ = the relaxation time,

α = the distribution (Cole-Cole) parameter,

and ω is an angular frequency, that is $\omega = 2\pi v$, with v being for the linear frequency in [Hz] units.[S1]

The results of the fittings according to the Debye model for a single relaxation process for **1md$^{\mathbf{HH}}$** are shown in Figures S13(*a–c*) and S14(*a–c*). The resulting relaxation times (τ) were plotted against *dc* magnetic field (Figure S13d) under constant temperature of 1.8 K, and against temperature (Figure S14d) under constant *dc* field of 400 Oe.

The τ versus H_{dc} dependence was fitted using the equation (e6):

$$\tau^{-1} = ATH^4 + a\left[\frac{(1+b^2H^2)}{(1+c^2H^2)}\right] \qquad \text{(e6)}$$

where the first term represented by the A parameter is related to the field-induced direct process, while the second term represented by the set of three parameters (a, b, c) is showing the contribution from quantum tunnelling of magnetization.[S2]

The fitting procedure performed for the τ versus H_{dc} dependence in **1md$^{\mathbf{HH}}$** (Figure S13d) at T = 1.8 K revealed that the A parameter of the direct process is very close to zero (A = 0), so as it was excluded. Therefore, results of the fitting for the τ versus H_{dc} dependence in **1md$^{\mathbf{HH}}$** (Figure S13d) at T = 1.8 K: a = 2988(105) s^{-1}, b = 7(1)·10^{-4} Oe^{-2}, and c = 0.0029(2) Oe^{-2}.

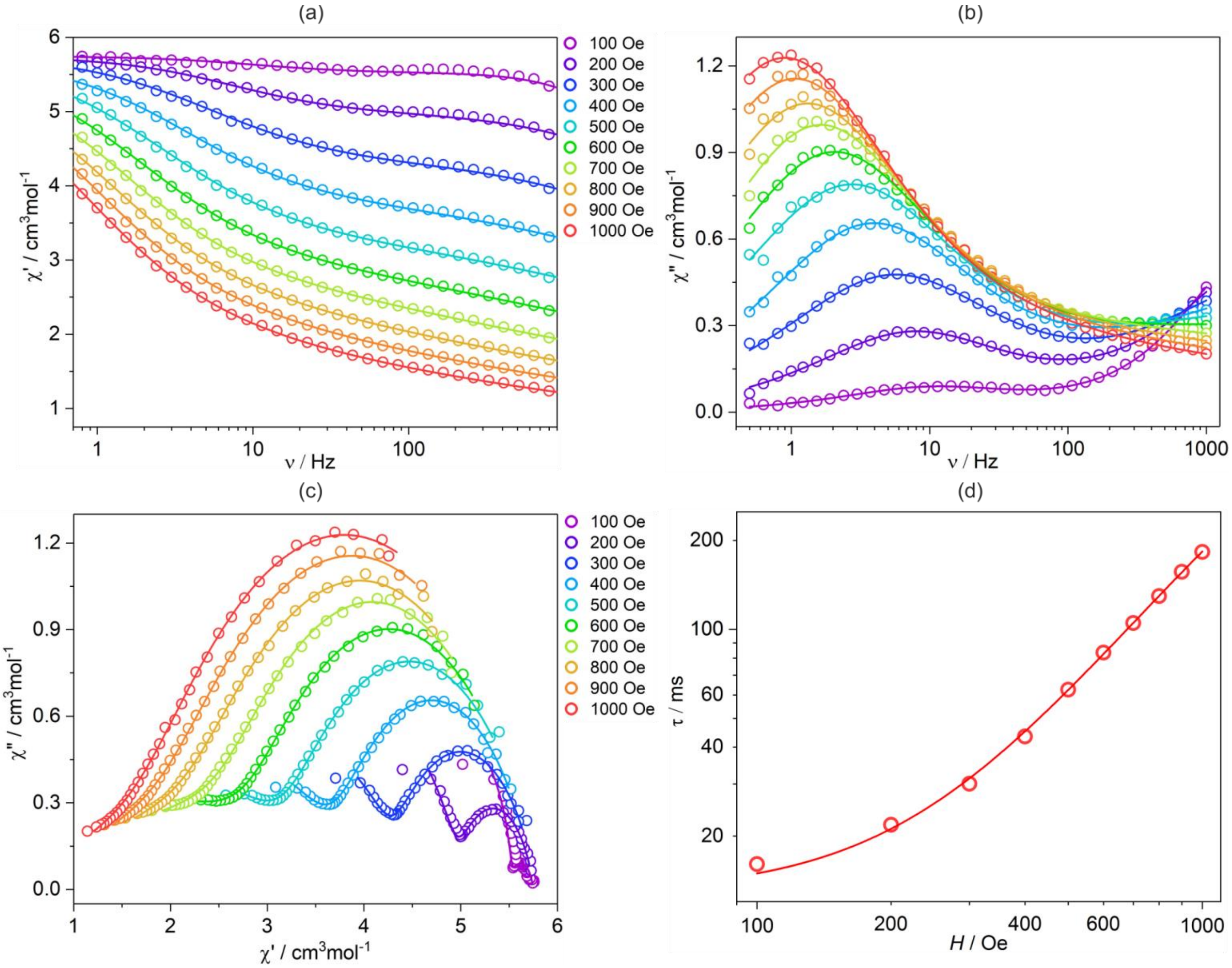

Figure S15. Complete magnetic-field-variable alternate-current (*ac*) magnetic susceptibility characteristics of $\mathbf{1}^{\mathbf{LH}}$ at T = 1.8 K, under H_{ac} = 1 Oe, and their analysis: frequency dependences of the in-phase susceptibility, χ' (*a*), and the out-of-phase susceptibility, χ'' (*b*) at various indicated *dc* external magnetic fields, together with the related Argand plots (*c*), and the field dependence of the relaxation time, τ (*d*). Both field and relaxation time were presented in (*d*) in the logarithmic scale. The relaxation times in (d) were shown for the slower, field-dependent relaxation process. Coloured solid curves in (*a*), (*b*), and (*c*) represent the best fits using the generalized Debye model for two relaxation processes (equations *e1* and *e2*). The solid line in (*d*) shows the best fit taking into account quantum tunnelling of magnetization, and a direct process in the range of 100–1000 Oe, following the equation (e3) (Page S17). The best-fit parameters are: A = 0 (fixed), a = 78(4) s^{-1}, b = 4.8(3)·10^{-4} Oe^{-2}, and c = 0.0041(3) Oe^{-2}.

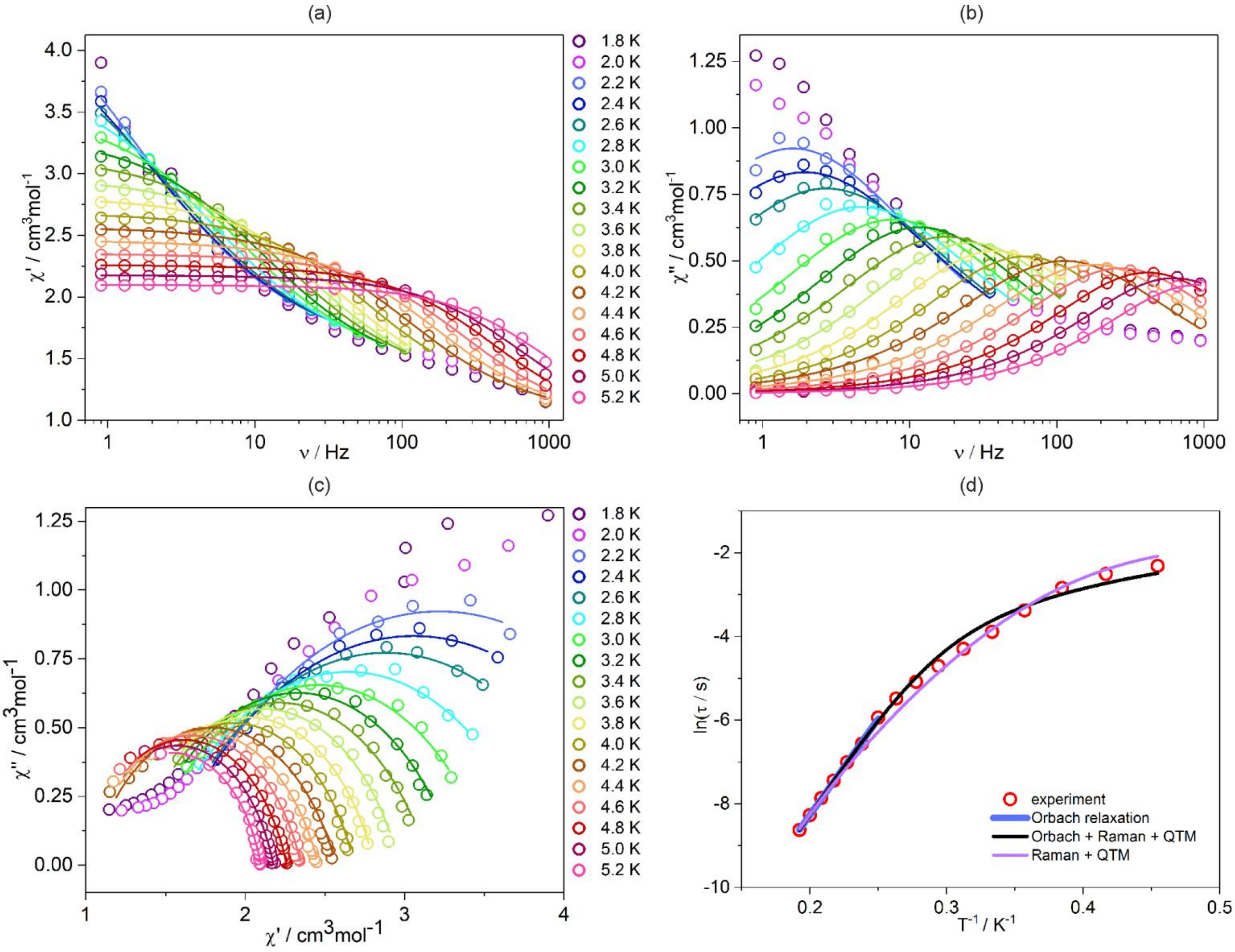

Figure S16. Complete temperature-variable alternate-current (*ac*) magnetic susceptibility characteristics of $\mathbf{1^{LH}}$ under H_{ac} = 1 Oe, H_{dc} = 1000 Oe, and their analysis: frequency dependences of the in-phase susceptibility, χ' (*a*), and the out-of-phase susceptibility, χ" (*b*) at various indicated temperatures, together with the related Argand plots (*c*), and the temperature dependence of the relaxation time, τ (*d*). Coloured solid curves in (*a*), (*b*), and (*c*) represent the best fits using the generalized Debye model for a single relaxation process. The solid blue line in (*d*) represents the linear fitting following the Arrhenius law ($\ln\tau = \ln\tau_0 - (U_{eff}/k_B)\cdot T^{-1}$) in the range of 4.0–5.2 K. The best-fit parameters are U_{eff}/k_B = 46.0(6) K with $\tau_0 = 2.6(3)\cdot 10^{-8}$ s. The black solid line in (*d*) shows the best fit taking into account the Orbach and Raman relaxation processes, and quantum tunnelling of magnetization (QTM), in the range of 2.2–5.2 K, while the direct process was excluded according to the fitting of the field-dependent *ac* magnetic data (Figure S15). Therefore, we followed the equation (e7):

$$\tau^{-1} = \tau_0^{-1}\exp(-U_{eff}/k_B T) + B_{Raman}T^n + \tau_{QTM}^{-1} \tag{e7}$$

where the first term with two fitting parameters (τ_0, U_{eff}/k_B) represents the Orbach thermal relaxation, the second term with two fitting parameters (B_{Raman}, n) indicates the Raman process, and the third term shows the contribution from the QTM effect (taken from field dependent *ac* data, Figure S15).[S1–S2] The best-fit parameters are: U_{eff}/k_B = 49.3(3) K, $\tau_0 = 1.5(2)\cdot 10^{-8}$ s, B_{Raman} = 0.18(6) $s^{-1}K^{-n}$, and n = 4.5(3), τ_{QTM} = 0.18(3) s (fixed). The violet solid line in (*d*) represents the best fit taking into account Raman process and QTM, without Orbach relaxation. The resulting parameters are B_{Raman} = 0.0022(3) $s^{-1}K^{-n}$, and n = 8.9(3), τ_{QTM} = 0.18(3) s (fixed).

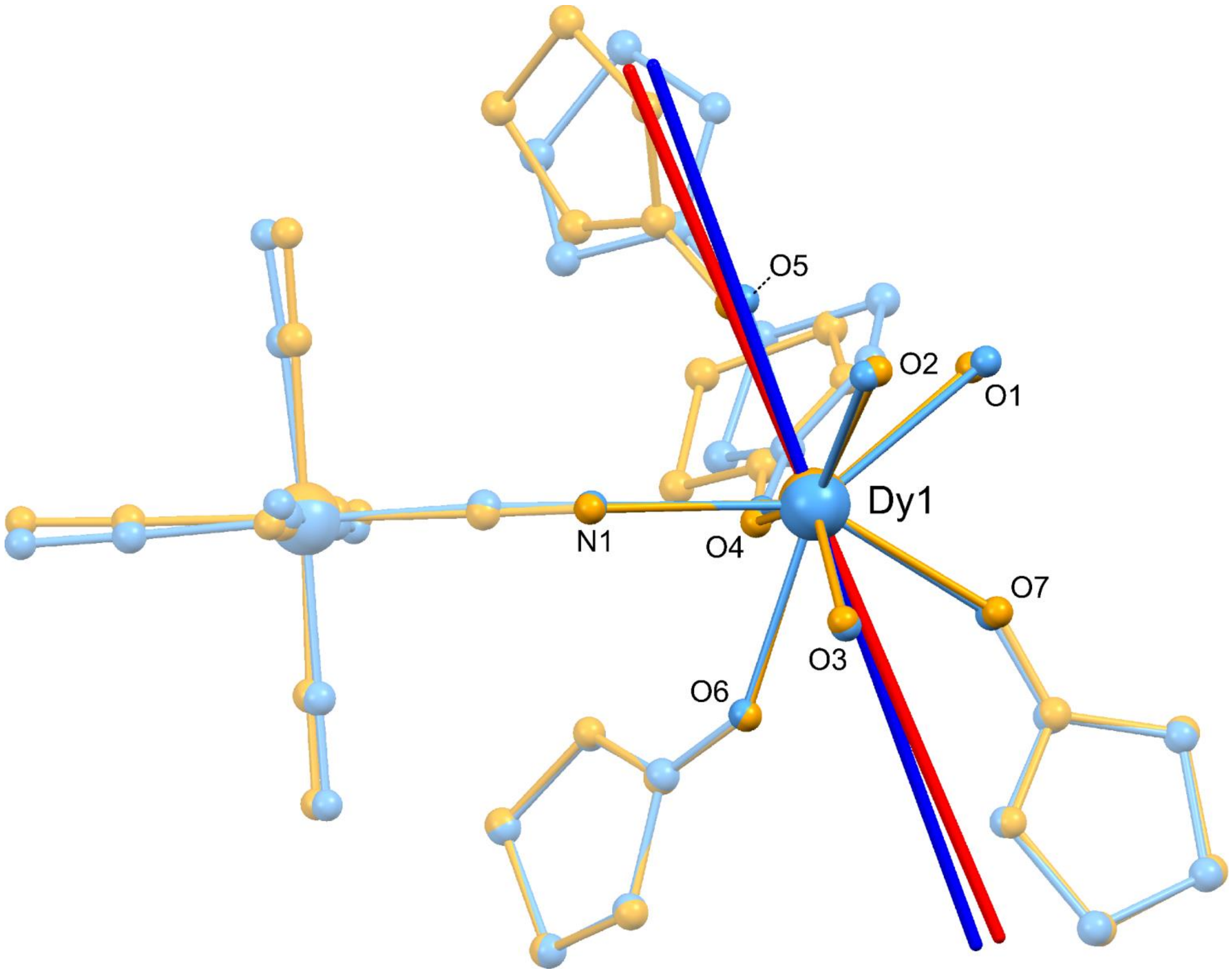

Figure S17. Visualization of Dy(III) magnetic easy axis directions in $\mathbf{1}^{\mathbf{HH}}$ (light blue structure, deep blue stick of anisotropy axis) and $\mathbf{1}^{\mathbf{LH}}$ (yellow structure, red stick of anisotropy axis). The magnetic anisotropy axes were obtained by using the electrostatic model within the MAGELLAN software,[S3] taking into account valence-bond-derived atomic charges for the surrounding ligands.[S4-S6]

[S3] N. F. Chilton, D. Collison, E. J. L. McInnes, R. E. P. Winpenny and A. Soncini, *Nat. Commun.*, 2013, **4**, 2551.

[S4] M. J. Davila, R. Alcalde and S. Aparicio, *Ind. Eng. Chem. Res.*, 2009, **48**, 1036.

[S5] F. Martin and H. Zipse, *J. Comput. Chem.*, 2005, **26**, 97.

[S6] M. F. C. Ladd, *J. Chem. Soc., Dalton Trans.*, 1977, 220.

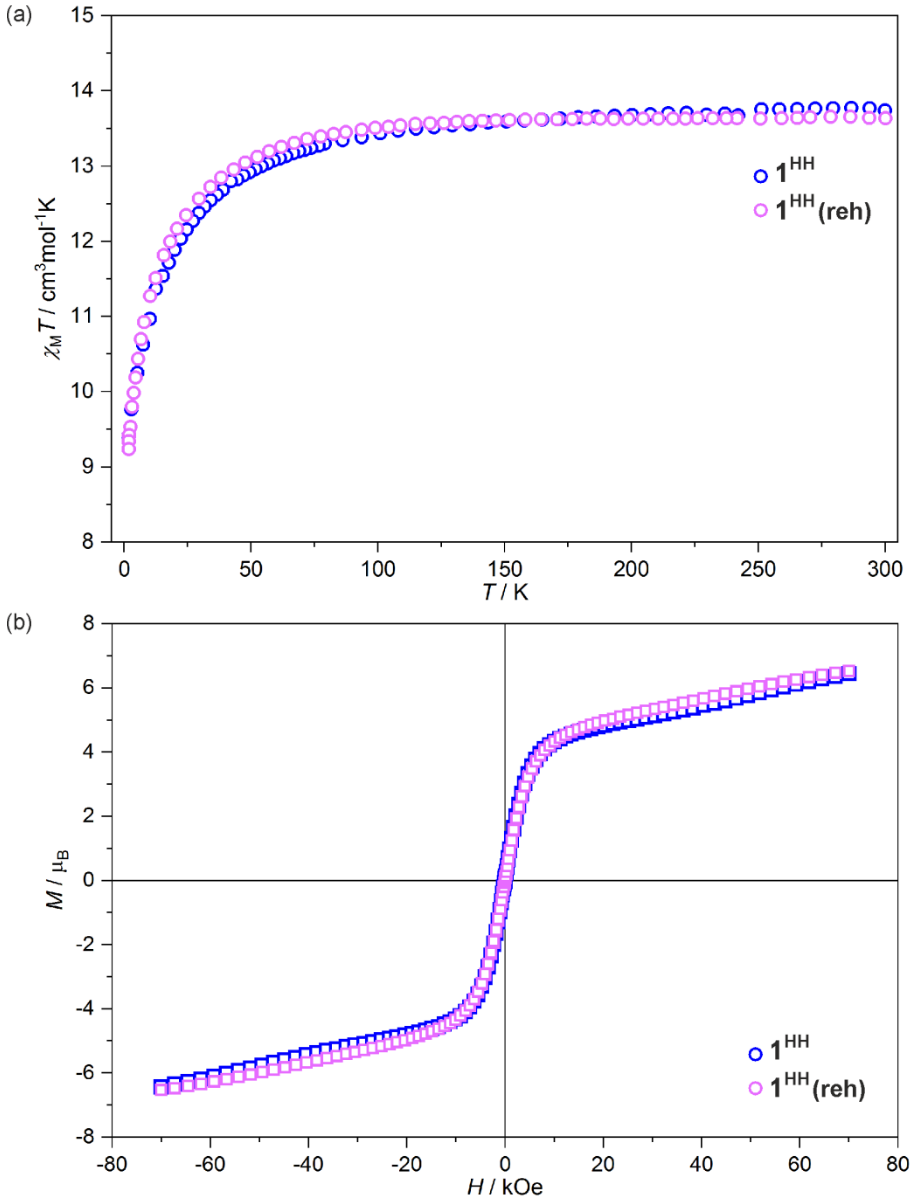

Figure S18. Direct-current (*dc*) magnetic properties of the rehydrated high humidity phase, $\mathbf{1^{HH}}$**(reh)** compared with the as-synthesized high humidity phase, $\mathbf{1^{HH}}$: the temperature dependence of the $\chi_M T$ product at H_{dc} = 1000 Oe (*a*), and the field dependence of molar magnetization, *M* at *T* = 1.8 K (*b*).

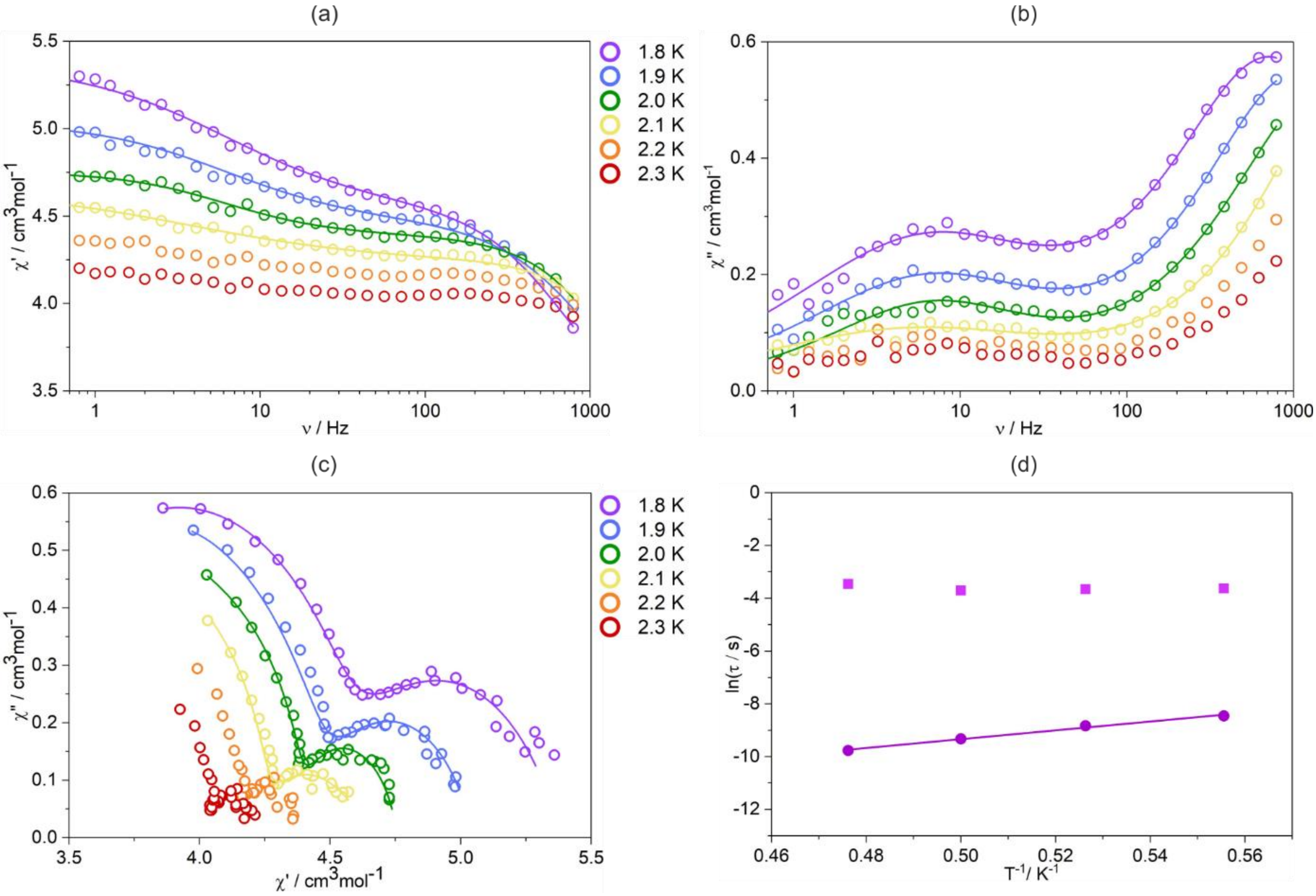

Figure S19. Complete temperature-variable alternate-current (*ac*) magnetic susceptibility characteristics of the rehydrated high humidity phase, $\mathbf{1^{HH}(reh)}$ under H_{ac} = 1 Oe, H_{dc} = 400 Oe, and their analysis: frequency dependences of the in-phase susceptibility, χ' (*a*), and the out-of-phase susceptibility, χ'' (*b*) at various indicated temperatures, together with the related Argand plots (*c*), and the temperature dependence of the relaxation time, τ (*d*). The relaxation times in (*d*) were shown for both the faster temperature-dependent relaxation (dark purple points), and the slower temperature-independent relaxation process (light purple points). Coloured solid curves in (*a*), (*b*), and (*c*) represent the best fits using the generalized Debye model for two relaxation processes (equations e1 and e2, Page S17). The solid line in (*d*) shows the best fit following the Arrhenius law ($\ln\tau = \ln\tau_0 - (\Delta E/k_B)\cdot T^{-1}$) in the range of 1.8–2.1 K. The best-fit parameters are U_{eff}/k_B = 17(1) K with $\tau_0 = 2.1(8)\cdot 10^{-8}$ s.

Table S6. Summary of the *ac* magnetic data for reported crystalline phases of **1**: high humidity phase, $\mathbf{1^{HH}}$, low humidity phase, $\mathbf{1^{LH}}$, magnetically diluted high humidity phase, $\mathbf{1md^{HH}}$, and rehydrated high humidity phase, $\mathbf{1^{HH}(reh)}$.

compound	$\mathbf{1^{HH}}$	$\mathbf{1^{LH}}$	$\mathbf{1md^{HH}}$	$\mathbf{1^{HH}(reh)}$
Field dependence of relaxation time[a]				
T [K]	1.8	1.8	1.8	-
A [$\mathrm{s^{-1}\,K^{-1}\,Oe^{-4}}$]	$4.4(3)\cdot10^{-9}$	0	0	-
a [$\mathrm{s^{-1}}$]	3513(177)	78(4)	2988(105)	-
b [$\mathrm{Oe^{-2}}$]	$4.6(9)\cdot10^{-8}$	$4.8(3)\cdot10^{-4}$	$7(1)\cdot10^{-4}$	-
c [$\mathrm{Oe^{-2}}$]	0.0015(2)	0.0041(3)	0.0029(2)	-
Temperature dependence of relaxation time[b]				
H_{dc} [Oe]	400	1000	400	400
B_{Raman} [$\mathrm{s^{-1}\,K^{-1}}$]	-	0.18(6)	-	-
n	-	4.5(3)	-	-
τ_0 [s]	-	$1.5(2)\cdot10^{-8}$	-	-
$U_{\mathrm{eff}}/k_{\mathrm{B}}$ [K]	-	49.3(3)	-	-
Temperature dependence of relaxation time Arrhenius plot[c]				
τ_0 [s]	$6.9(8)\cdot10^{-8}$	$2.6(3)\cdot10^{-8}$	$8.4(9)\cdot10^{-8}$	$2.1(8)\cdot10^{-8}$
$U_{\mathrm{eff}}/k_{\mathrm{B}}$ [K]	**15.6(4)**	**46.0(6)**	**16.3(7)**	**17(1)**

[a] Results of fitting the field-dependence of relaxation time (equation e3, Page S17). [b] Results of fitting the temperature-dependence of relaxation time (equation e7, Page S23), using the parameters of A, a, b, and c from fitting of the field-dependence. [c] Results of fitting to the Arrhenius law.

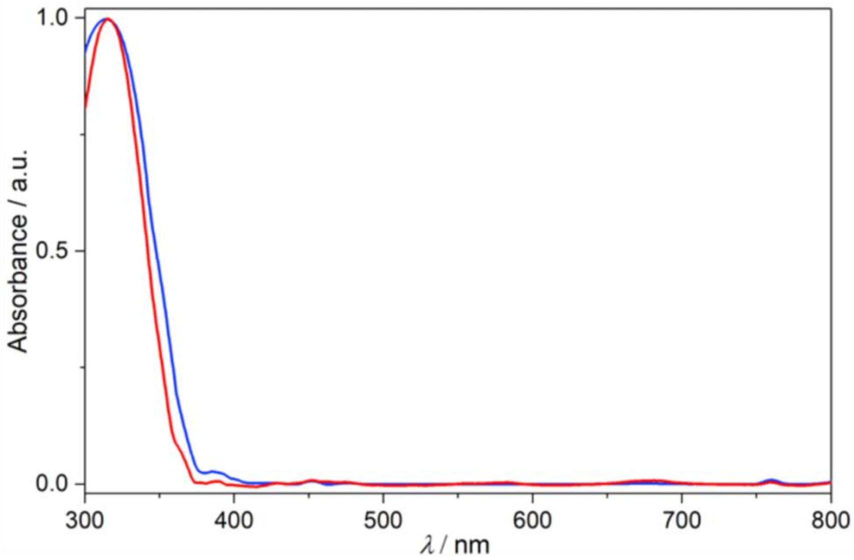

Figure 20. UV-Vis-NIR solid state absorption spectra of $\mathbf{1}^{\mathbf{HH}}$ (blue) and $\mathbf{1}^{\mathbf{LH}}$ (red).

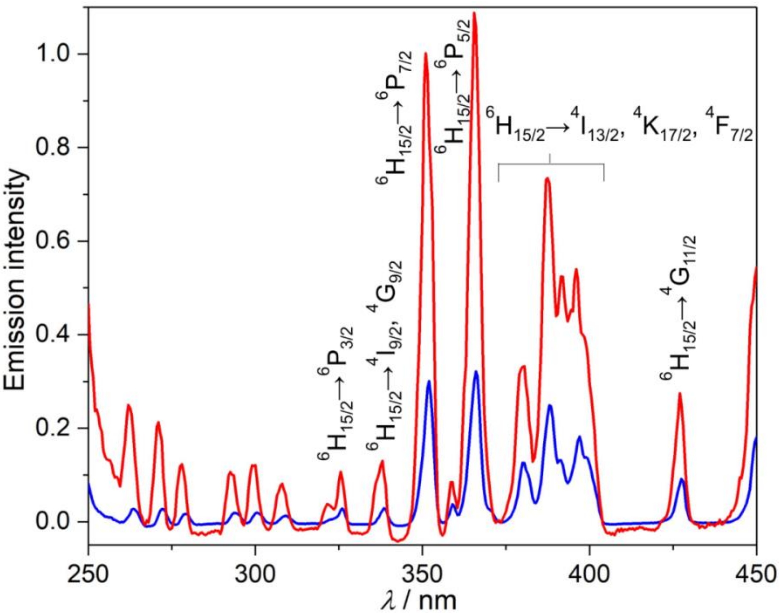

Figure S21. Solid state excitation spectra of $\mathbf{1}^{\mathbf{HH}}$ (blue) and $\mathbf{1}^{\mathbf{LH}}$ (red) at the monitored emission wavelength of 572 nm, gathered at the temperature of 77 K. The main Dy(III)-centred electronic transitions are indicated on the graph.

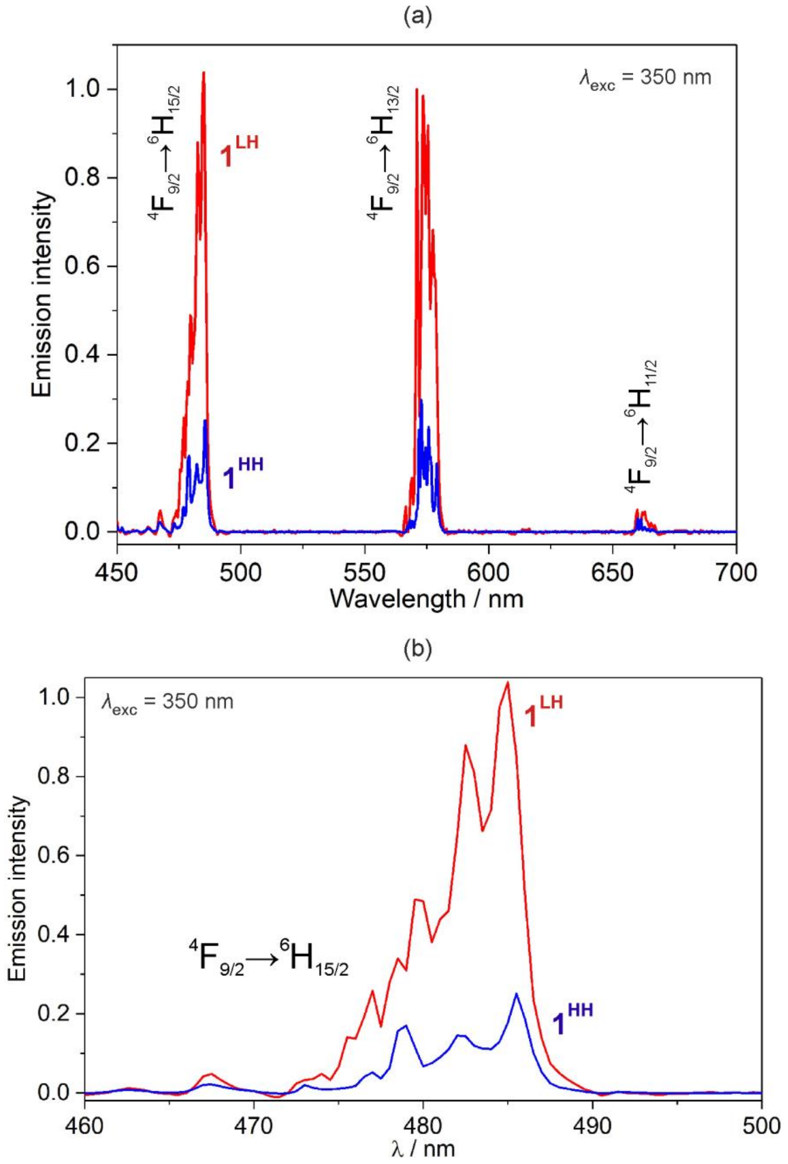

Figure S22. Solid state emission spectra of $\mathbf{1^{HH}}$ (blue) and $\mathbf{1^{LH}}$ (red) gathered at the low temperature of 77 K (*a*) with the enlargement of the bands related to the $^4F_{9/2}\rightarrow{}^6H_{15/2}$ electronic transition (*b*). The spectra were gathered for the analogous amounts of the powder samples. Instrument background correction was introduced but the intensity was then left without further scaling. It roughly shows the increase of the overall emission intensity going from $\mathbf{1^{HH}}$ (blue) to $\mathbf{1^{LH}}$ (red).